J. Phys. Soc. Jpn.
Downloaded from journals.jps.jp by 138.25.168.236 on 11/21/22

Journal of the Physical Society of Japan **91**, 084802 (2022)
https://doi.org/10.7566/JPSJ.91.084802

High-Pressure Synthesis of High-Entropy Metal Disulfides with Pyrite-Type Structure

Anna Z. Laila[1], Marco Fronzi[1], Shinya Kumegai[1], Kazumasa Sugiyama[2],
Ryota Furui[1], and Ayako Yamamoto[1]*

[1]*Graduate School of Science and Engineering, Shibaura Institute of Technology, Koto, Tokyo 135-8548, Japan*
[2]*Institute of Materials Research, Tohoku University, Sendai 980-8577, Japan*

(Received March 31, 2022; accepted June 6, 2022; published online July 21, 2022)

We succeed in synthesizing equimolar-multi metal solid solutions of (Fe, Co, Ni, Cu)S_2 and (Fe, Co, Ni, Cu, Ru)S_2 by sintering at 900 °C under 2–4 GPa. These were stabilized by the high-entropy effect. Nevertheless, (Fe, Co, Ni, Cu, M)S_2 (M = Zn, Mn, or Cd) was not obtained as single phase under the same synthetic conditions, mostly owing to the relatively large ionic radius of M^{2+}. Single-crystal X-ray diffraction analysis shows that (Fe, Co, Ni, Cu)S_2 crystallizes into a pyrite type with the space group $Pa\bar{3}$ (#205) [$a = 5.777(3)$ Å], randomly distributed at one site. The results of electrical resistivity and magnetic *dc*-susceptibility measurements indicate that both (Fe, Co, Ni, Cu)S_2 and (Fe, Co, Ni, Cu, Ru)S_2 are metals with ferrimagnetic ordering below $T_c = 130$ K. The band structure and the projected density of states (Fe, Co, Ni, Cu)S_2, were obtained by density functional theory calculations in a high-entropy representative supercell, supporting the experimental results.

1. Introduction

High-entropy alloys (HEAs) are crystal structures that contain typically five or more elements with a nearly equal atomic ratio.[1,2] According to the Gibbs free energy (G) equation, $\Delta G = \Delta H - T\Delta S$ (H: enthalpy, T: temperature, and S: entropy), the high configurational mixing entropy ($\Delta S_{mix} = -R\sum_i x_i \ln x_i$, where R is gas constant and x is a compositional ratio) decreases the Gibbs free energy and stabilizes the formation of solid solution at high temperature.[2] The same concept can be extended to a wide range of materials. Because of the high-entropy structure, HEAs exhibit physical properties, such as high corrosion resistance, high hardness, high strength, distorted lattices, and slow diffusion, that can be useful in many technological applications.[2,3]

Currently, there are several examples of high-entropy compounds and the analysis of their physical and chemical properties in the literature.[4–10] Rost et al. reported entropy stabilized oxides (Mg, Co, Ni, Cu, Zn)O with the NaCl-type structure in 2015,[4] and subsequently, several high-entropy oxides such as Li-doped NaCl types[5] and pyrochlore types[6] were synthesized. Afterwards, a few metal sulfides were studied (e.g., $Cu_5SnMgGeZnS_9$) as promising thermoelectric materials owing to the atomic disorders that reduce their thermal conductivity.[7–10] Disulfides, MS_2, with pyrite type (Fe, Ni, Co, Cr, M)S_2 (M = Mn, Cu, Zn or Al)[8] and (Fe, Mn, Ni, Co, M)S_2 (M = Ti, Cr, Cu)[9] were studied as environmentally functional materials for high-performance oxygen-evolution reactions and Li-battery electrodes. Both can form fine powders with low crystallinity or that are partially amorphous when produced by solvothermal synthesis at a low temperature and mechanochemical synthesis at room temperature, respectively.[8,9] Likewise, the CdI_2 type represents another typical MS_2 structure with properties typical of high-entropy sulfides, (Ti, V, Cr, Nb, Ta)S_2.[10]

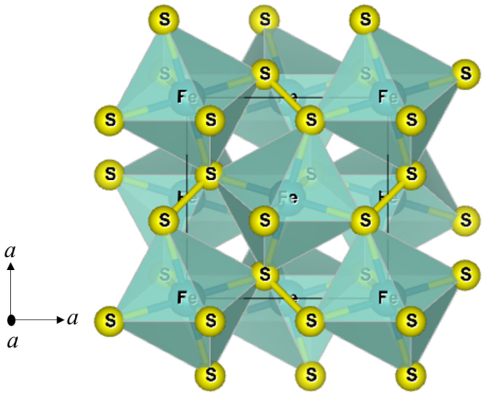

Fig. 1. (Color online) Crystal structure model of pyrite, FeS_2, visualized using VESTA software.

Pyrite, FeS_2, is the most abundant mineral sulfide, and its structure is common among metal disulfides MS_2.[11] It crystallizes into space group $Pa\bar{3}$ (#205) where FeS_6 octahedra are connected three-dimensionally with corner sharing, and the anion unit of S_2 dimers occupies the Cl site in the NaCl-type structure, as shown in Fig. 1.[12] The bond distance between sulfurs in the dimer could be determined using the one atomic positional parameter that indicates the degree of covalency, as discussed for IrS_2.[13] This could be a key point in understanding the structure of pyrite compounds. The 3d-transition metal disulfides, MS_2, crystallize into a pyrite-type structure under different environmental conditions. For example, metal sulfides containing Mn and Ni form the pyrite-type structure at ambient pressure, whereas Cu and Zn do only at high pressure.[14] The configuration of d electrons in MS_2 pyrites is crucial in the determination of the electrical transport and magnetic properties of the compound.[15] MnS_2 with a high-spin configuration ($t_{2g}^3 e_g^2$) and FeS_2, CoS_2, and NiS_2 with a low-spin configuration ($t_{2g}^6 e_g^0$, $t_{2g}^6 e_g^1$, and $t_{2g}^6 e_g^2$) respectively are an antiferromagnetic (T_N = 48.2 K)[15] semiconductor (E_g = 1.3 eV),[16] a diamagnetic semiconductor (E_g = 0.8 eV),[15] a ferromagnetic (T_c = 120 K) metal,[17] and an antiferromagnetic (T_N = 40 K) insulator.[18] In contrast to the high-pressure phases of CuS_2 and ZnS_2 are superconductors (T_c = 1.50 K)[19] and semiconductors (E_g ~ 2.5 eV).[20] Both RuS_2[21] and CdS_2, with the same electronic configurations as FeS_2 and ZnS_2, respec-

©2022 The Author(s)

This article is published by the Physical Society of Japan under the terms of the Creative Commons Attribution 4.0 License. Any further distribution of this work must maintain attribution to the author(s) and the title of the article, journal citation, and DOI.

J. Phys. Soc. Jpn.
Downloaded from journals.jps.jp by 138.25.168.236 on 11/21/22

tively, are semiconductors. The properties of these pyrites have been of great scientific interest.[20] However, only a detailed analysis of the physical properties of two elements in solid solution has been reported,[22] and there is no report of high-entropy compounds with a larger number of elements in solid solution, where exotic properties may appear owing to a possible multiple-element interaction.

Here, we report the structural and physical properties of equimolar four- and five-metal solid solutions, (Fe, Co, Ni, Cu)S_2 and (Fe, Co, Ni, Cu, Ru)S_2, in high-entropy compounds with pyrite-type structures. To obtain homogenous and well-crystallized samples, we used a high-pressure approach. This method has the advantages of the suppression of highly volatile off-stoichiometry elements (i.e., sulfur),[23] high reactivity accompanied with high compressibility, and the possibility of a quick quench during sintering. In particular, the quenching procedure has been found to be a critical aspect in to obtain high-entropy compounds in a metastable phase. In this study, we successfully synthesized both poly- and single-crystalline samples of (Fe, Co, Ni, Cu)S_2 and (Fe, Co, Ni, Cu, Ru)S_2, and we investigated the crystal structure together with their physical and chemical properties. The results of our experimental analysis show that these materials are metallic with a ferrimagnetic character, which is also confirmed by our density functional theory (DFT) calculations.

2. Methodology

The samples are prepared from a mixed powder of FeS (99%), CoS (99%), NiS (99.9%), Cu_2S (99%), ZnS (99.99%), Ru (99.9%), Mn (99.99%), Cd (99%), and S (99.99%) with the composition of MS_2 (M is 3–5 selected equimolar metals) using 180-ton (2–4 GPa) and 500-ton (5–7.5 GPa at RIKEN Institute) cubic anvil-type high-temperature–high-pressure presses (Try Engineering). The samples were preheated at 500 °C for 30 min as a calcination process of metal disulfides and sintered at 900–950 °C for 30 min, then quenched to room temperature in one min under high pressure.

The samples were identified and characterized using an X-ray powder diffractometer (CuKα) with a Johansson-type monochromator to cut CuKα_2 (Rigaku SmartLab). The unit cell parameters were calculated by the conventional Rietveld method using the diffraction patterns. The crystal morphology was observed by scanning electron microcopy (SEM) (JEOL JCM-6000 Plus). We used the diffractometer XtaLAB Synergy, Dualflex Hypic Numerical for X-ray diffraction single-crystal measurement. Then, the data collection, cell parameter refinement, and data reduction of a single crystal were carried out using the processing software *CrysAlis PRO* (Rigaku OD, 2021).[24] The phase structure was identified using SHELXT (Sheldrick, 2015a)[25] and the refinement process was performed using SHELXL-14 (Sheldrick, 2015b).[26]

The temperature dependence of electrical resistivity was measured by the four-terminal method at 5–300 K (Quantum Design PPMS). The temperature dependence (10–300 K) and the field dependence (−0.5 T–+0.5 T) of *dc*-susceptibility were measured using the SQUID (Quantum Design MPMS).

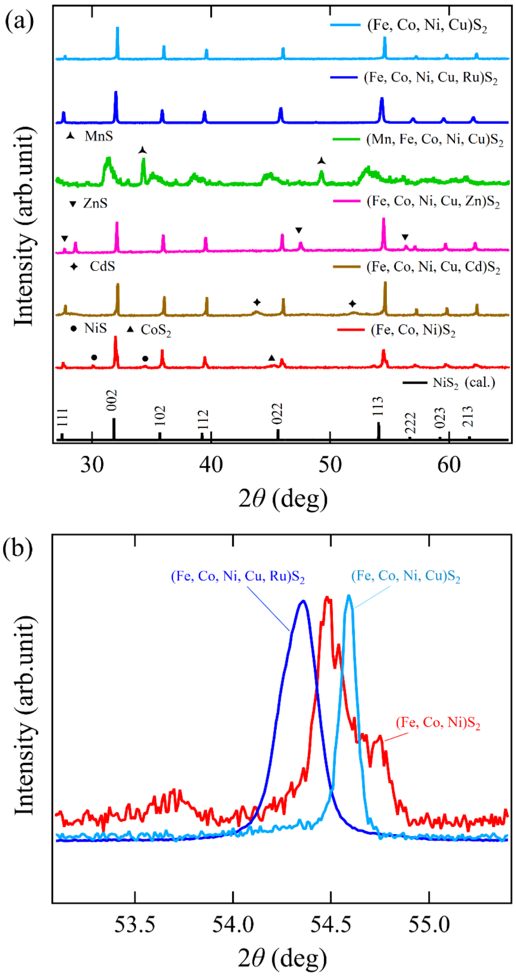

Fig. 2. (Color online) (a) X-ray diffraction patterns of three-, four-, and five-metal equimolar disulfides MS_2 (M = Mn, Fe, Co, Ni, Cu, Ru). (b) Peak profiles of 113 diffraction of (Fe, Co, Ni)S_2, (Fe, Co, Ni, Cu)S_2, and (Fe, Co, Ni, Cu, Ru)S_2.

The band structure and density of states of (Fe, Co, Ni, Cu)S_2 were calculated by applying the density functional theory using a VASP simulation package, wherein the core valence interaction is described by the projected augmented wave pseudopotential. The calculations presented here were carried out within the generalized gradient approximation (GGA) using the Perdew–Burke–Enzerhof functional (PBE) for the exchange–correlation term. We included a Hubbard correction with U (Ni3d) = 6.38 eV to reproduce the antiferromagnetic order in NiS_2 reported in the literature.[27] We used a cut-off energy of 520 eV for the valence electrons and a $(3 \times 3 \times 3)$ k-point mesh for the supercell consisting of 96 atoms, which was built by merging eight primitive cells along the x–y–z directions and randomizing the positions of Fe, Co, Ni, and Cu at the cation sites. Full geometry optimization including spin polarization was performed with the energy minimization tolerance of 10^{-6} eV and the force tolerance of 10^{-2} eV/Å.

3. Results and Discussion

We synthesized the samples under pressure of 2–4 GPa at sintering temperature of 900–950 °C using different combinations of 3–5 selected equimolar metals MS_2 (M = Fe, Co, Ni, Cu, Zn, Ru, Mn, and Cd) with addition/subtraction to/from (Fe, Co, Ni, Cu)S_2. Figure 2(a) shows X-ray powder diffraction (XRD) patterns of the samples. Single phases of (Fe, Co, Ni, Cu)S_2 and (Fe, Co, Ni, Cu, Ru)S_2 were obtained,

©2022 The Author(s)

J. Phys. Soc. Jpn.
Downloaded from journals.jps.jp by 138.25.168.236 on 11/21/22

while impurities were found in the versions with added Zn, Cd, or Mn. We expected single-phase formation in the Zn-added version because NaCl-type (Mg, Co, Ni, Cu, Zn)O was stabilized as a high-entropy phase in a simple 3*d*-transition metal (except Mg) oxide. However, ZnS was very stable and did not show any reaction to pressure up to 7.5 GPa at 950 °C. In the current work, higher pressure and higher temperature lead to a decomposition of the pyrite phase itself, although ZnS$_2$ is reported to be stabilized at 6.5 GPa.[20] The Cd-included version of the crystal [i.e., (Fe, Co, Ni, Cu, Cd)S$_2$] shows a trend that is similar to that of the Zn-added version, while the Mn-added version formed a multiphase without any clear pyrite phase. For mechanochemical synthesis in (Fe, Mn, Ni, Co, M)S$_2$ (M = Ti, Cr, Cu), Mn was incorporated into the pyrite phase.[9] This discrepancy suggests that the phase stability of high-entropy compounds is significantly affected by the synthesis conditions (methods, temperature, and pressure).

Upon the elimination of one element from (Fe, Co, Ni, Cu)S$_2$, we observed that the phases did not crystallize into a solid solution. The same procedure was repeated for any combination of three-metal equimolar solid solutions, (Fe, Co, Ni)S$_2$, (Co, Ni, Cu)S$_2$, (Fe, Ni, Co)S$_2$, and (Fe, Co, Cu)S$_2$. As shown in Fig. 2(b), the second intense peak near $2\theta = 54°$ of (Fe, Ni, Co)S$_2$ seems to overlap with several other peaks, whereas there is no overlap in (Fe, Co, Ni, Cu)S$_2$ or (Fe, Co, Ni, Cu, Ru)S$_2$. This result suggests that single-phase formation is correlated with the number of elements, i.e., the degree of randomness. Furthermore, whether a single phase could be obtained or not also depends on the ionic radius of the additional element. The radii of Cd (2+ and CN = 6 the same applies hereafter, 0.95 Å) and Mn [0.83 Å (high-spin)] are much larger than those of Fe (0.65 Å), Co (0.61 Å), Ni (0.69 Å), and Ru (0.62 Å),[28] indicating that the mismatch of ionic radii also inhibits single-phase solid solution formation. However, although the radii of Zn (0.74 Å) and Cu (0.73 Å)[28] are close to each other, the high stability of ZnS owing the closed shell of Zn may make this reactant inert. The lattice parameters of (Fe, Co, Ni, Cu)S$_2$ and (Fe, Co, Ni, Cu, Ru)S$_2$ determined by powder XRD analyses are a = 5.5794(2) and 5.60152(19) Å, respectively. The sharper peak profile of (Fe, Co, Ni, Cu)S$_2$ indicates the higher crystallinity of the sample [see Fig. 2(b)].

To test the stability of high-pressure phases, we annealed the samples at ambient pressure with flowing nitrogen gas. A pyrite single phase of (Fe, Co, Ni, Cu)S$_2$ decomposed into pyrite-type phases and the NiAs-type phase after annealing at 400 °C. The phase of the sample prepared at high pressure was not stable at ambient pressure and temperature, suggesting that our samples were stabilized mainly by the high-entropy effect. We also observed that the three-metal equimolar solid solution could not be stabilized into a pyrite single phase under the same synthesis conditions as used for four- and five-metal equimolar solid solutions (P = 4 GPa, T = 900 °C).

The extraction of single crystals from a bulk sample is another advantage of the high-pressure syntheses of the compounds. The sample melts during heating and crystallizes during cooling. To obtain relatively large crystals of about 20–40 μm for the X-ray diffraction analysis, a slow cooling rate from 950 to 800 °C (for 2 h) was used, followed by a quick quench within approximately 1 min. Figure 3 shows an SEM image of a cross section of the bulk sample with one of the typical morphologies of the cubic phase.

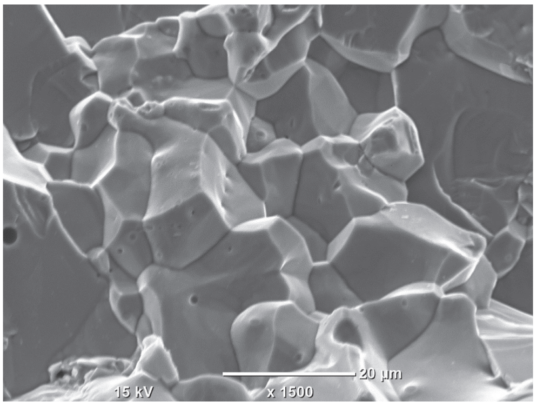

Fig. 3. SEM image of cross section of (Fe, Co, Ni, Cu)S$_2$.

Table I. Structural parameters refined by X-ray single crystal diffraction analysis of (a) (Fe, Co, Ni, Cu)S$_2$ and (b) FeS$_2$ (Mineral). Space group is $Pa\bar{3}$ (#205) with a = 5.5777(3) and 5.42094(9) Å, respectively.

(a) (Fe, Co, Ni, Cu)S$_2$

Atom	Position	Occupancy	X	Y	Z	U_{iso} (Å^2)
M^*	4*b*	1*	0	0	$\frac{1}{2}$	0.00659(6)
S	8*c*	1	0.39137(4)	X	X	0.00697(7)

(b) FeS$_2$ (Mineral)

Atom	Position	Occupancy	X	Y	Z	U_{iso} (Å^2)
Fe	4*b*	1	0	0	$\frac{1}{2}$	0.00355(6)
S	8*c*	1	0.38482(4)	X	X	0.00435(8)

$^*M$: fixed as Fe$_{1/4}$Co$_{1/4}$Ni$_{1/4}$Cu$_{1/4}$

We studied the crystal structure of a four-metal equimolar solid solution, (Fe, Co, Ni, Cu)S$_2$ using the X-ray single-crystal diffraction analysis system, SHELXL-2014,[26] together with a FeS$_2$ mineral crystal as a reference. Measured positional parameters are shown in Table I and the experimental details are listed in Table S1.[29] The structures of (Fe, Co, Ni, Cu)S$_2$ and FeS$_2$ are the pyrite type with space group $Pa\bar{3}$ (#205) and lattice parameters a = 5.5777(3) and 5.42094(9) Å, respectively. The x (in 8*c* site) of (Fe, Co, Ni, Cu)S$_2$ [0.39137(4)] is larger than that of FeS$_2$ [0.38482(4)], and this corresponds to the S–S distance, which will be discussed later. U_{iso} of (Fe, Co, Ni, Cu)S$_2$ [0.00659(6) Å^2] is also larger than that of Fe [0.00355(6) Å^2] in FeS$_2$. This could be interpreted to mean that the atomic disorder or thermal vibration is enhanced by the high-entropy effect,[30] while the value of (Fe, Co, Ni, Cu)S$_2$ is close to that of U_{iso} for Cu [0.00732 Å^2] in CuS$_2$ of the single-metal pyrite.[14] The results indicate that the positional disorder of (Fe, Co, Ni, Cu)S$_2$ is considerably suppressed, which suggests that this solid solution is stabilized by the high-entropy effect. Unfortunately, the crystal size of (Fe, Co, Ni, Cu, Ru)S$_2$ was not large enough to allow a diffraction analysis. Further crystallographic study using single crystals is needed to gain significant conclusions.

To analyze the interatomic distances of (Fe, Co, Ni, Cu)S$_2$ and mono-metal disulfides, we plot the unit cell parameters and bond distances of M–S and S–S in MS$_2$ versus ionic radii of our analysis, together with the reported ones of 3*d*-

©2022 The Author(s)

J. Phys. Soc. Jpn.
Downloaded from journals.jps.jp by 138.25.168.236 on 11/21/22

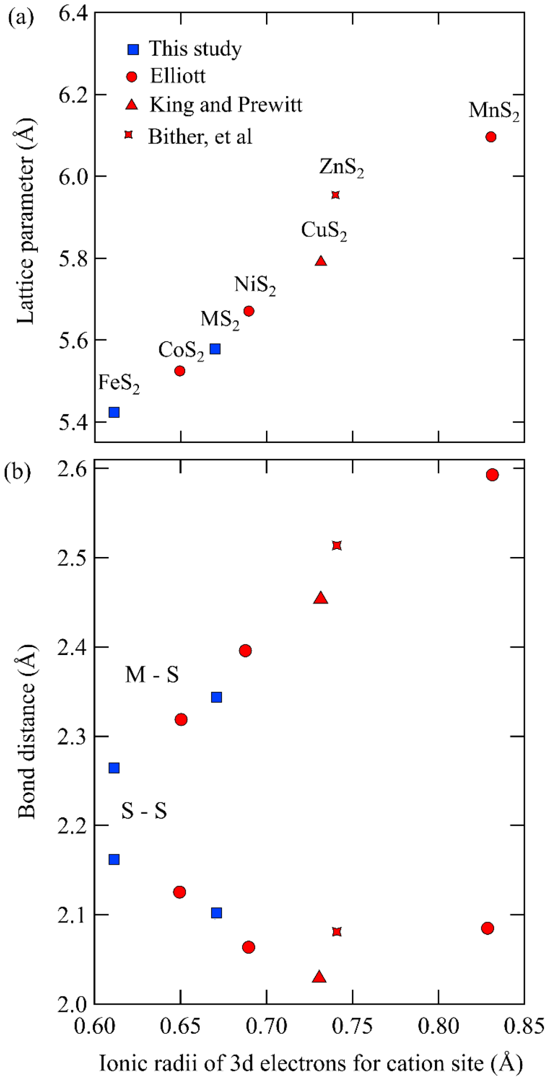

Fig. 4. (Color online) Lattice parameters and bond distances versus ionic radii of the $3d$-transition metal disulfides with pyrite structure including MS_2 (M = Fe, Co, Ni, Cu), together with reported values.

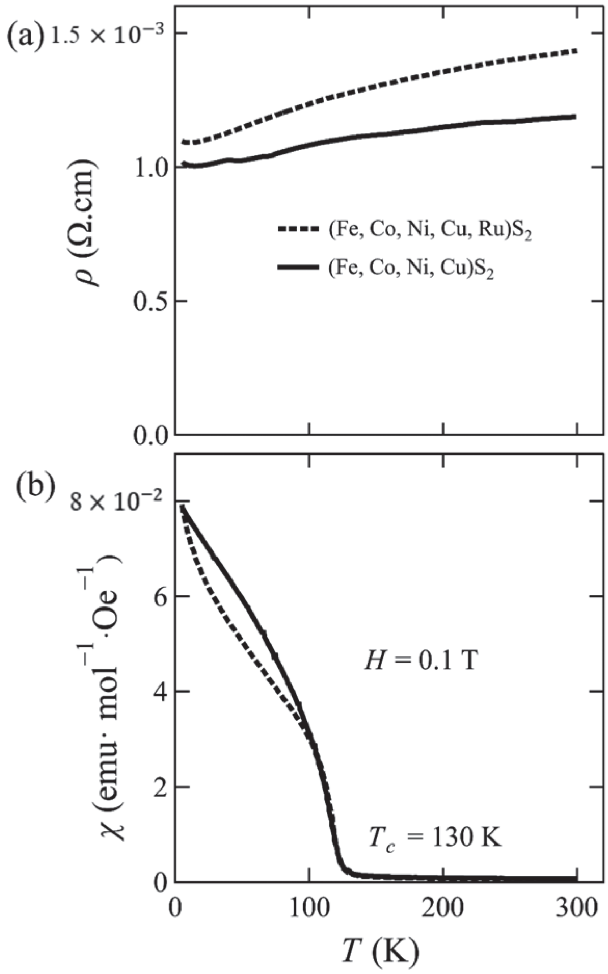

Fig. 5. (a) Temperature dependence of electrical resistivity $\rho(T)$ and (b) temperature dependence of dc-magnetic susceptibility $\chi(T)$ of (Fe, Co, Ni, Cu)S$_2$ and (Fe, Co, Ni, Cu, Ru)S$_2$.

transition metals, in Fig. 4. Both unit cell parameter, a, and the bond distance of M–S monotonically increase with increasing ionic radii except for Zn.[13] The values of (Fe, Co, Ni, Cu)S$_2$ fall between those of Co and Ni, and correspond to an averaged ionic radius of [Fe (0.65 Å), Co (0.61 Å), Ni (0.69 Å), and Cu (0.73 Å)].[28,31] On the other hand, the S–S distance decreases with increasing metal ionic radius, with longer distances in Zn and Mn. The S–S distance of (Fe, Co, Ni, Cu)S$_2$ also follows a linier relationship that obtained in the other pyrites MS_2 (M = Fe, Co, Ni, Cu); therefore, we could estimate the covalency degree among them. According to Jobic et al., the S–S distance in dimer corresponds to its covalency, and a short distance indicates higher covalency.[13]

The temperature dependences of electrical resistivity, $\rho(T)$, were measured for polycrystalline samples of (Fe, Co, Ni, Cu)S$_2$ and (Fe, Co, Ni, Cu, Ru)S$_2$. The resistivities were as high as 1×10^{-3} Ωcm at 300 K, as shown in Fig. 5(a). They are not as low as that of metal but are sufficient to determine metallic conductivity with a resistivity that decreases with decreasing temperature. It is unclear why the residual resistivity ratio (RRR) is so low, but it may be that the structural disorder induced by the inclusion of multiple metals may lead to a complicated band structure, as shown in the next section.

Figure 5(b) shows the temperature dependence of magnetic dc-susceptibility, $\chi(T)$, of (Fe, Co, Ni, Cu)S$_2$ and (Fe, Co, Ni, Cu, Ru)S$_2$ in a field of 1000 Oe. There is a negligible temperature dependence with a low susceptibility associated with paramagnetism at 300–130 K. On the other hand, the magnetic susceptibility peak increases below 130 K in both (Fe, Co, Ni, Cu)S$_2$ and (Fe, Co, Ni, Cu, Ru)S$_2$, indicating ferro- or ferrimagnetism. We plotted inverse magnetic susceptibility versus temperature, $1/\chi(T)$, and fitted the curve in the paramagnetic region at $T = 180$–300 K to the Curie–Weiss Law, $\chi = C/(T - \theta_p)$, where C is the Curie constant and θ_p is the Weiss temperature (see Fig. S1).[32] The θ_p was -124.20 and -51.30 K, for (Fe, Co, Ni, Cu)S$_2$ and (Fe, Co, Ni, Cu, Ru)S$_2$, respectively. The negative values of θ_p suggest that antiferromagnetic coupling is predominant, and the shape of the curve of $1/\chi(T)$ below $T = 180$ K suggests ferrimagnetic ordering. The effective magnetic moment, μ_{eff}, is 1.55 and 1.25 μ_B per metal ion for (Fe, Co, Ni, Cu)S$_2$ and (Fe, Co, Ni, Cu, Ru)S$_2$, respectively.

The M–H loop exhibits extremely weak hysteresis and low coercive force, suggesting a possible ferrimagnetic order in the soft magnetic category. The saturated magnetizations (M_s) are 0.0140 and 0.0167 μ_B per formula unit for (Fe, Co,

©2022 The Author(s)

J. Phys. Soc. Jpn.
Downloaded from journals.jps.jp by 138.25.168.236 on 11/21/22

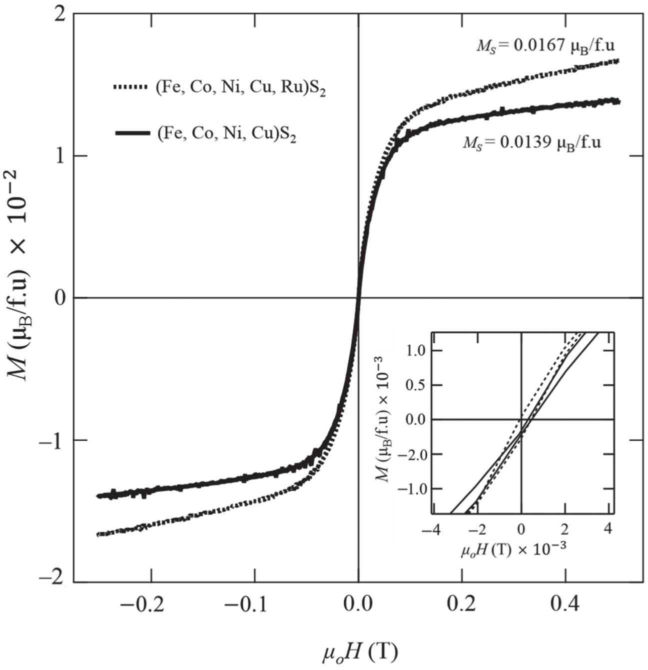

Fig. 6. Applied-magnetic-field-dependent magnetization $M(H)$ at $T = 10$ K with magnetic field of −0.5 T–+0.5 T for (Fe, Co, Ni, Cu)S$_2$ and (Fe, Co, Ni, Cu, Ru)S$_2$.

Ni, Cu)S$_2$ and (Fe, Co, Ni, Cu, Ru)S$_2$, respectively, as shown in Fig. 6. These values are approximately only 1% of the assumed full moment for each metal, $S \sim 1.5\,\mu_B$, which we calculated from the average theoretical magnetic spin, $\mu_s = \mu_{eff}$, of (Fe^{2+}, Co^{2+}, Ni^{2+}, and Cu^{2+}) obeying Hund's rule, $2[S(S+1)]^{1/2}$ for $3d$ transition metal octahedral complexes.[33] We expect low M_s because of the large contribution of aligned antiparallel spin, which is explained further in the next discussion. In addition, we also find that the μ_{eff} values of theoretical and experimental calculations are approximately the same. We applied magnetic field up to 50,000 Oe, but no additional enhancement owing to spin ordering was observed.

The band structure and density of states (DOS) of (Fe, Co, Ni, Cu)S$_2$ were calculated on the basis of DFT using the structural data of single-crystal XRD analysis as the starting point of optimization of the crystal model shown in Fig. 7. We assumed that four metals randomly occupy at one crystallographic site in the cubic system. The electronic band structure is shown in Fig. 8(a), where the energy difference between spin-up and spin-down channels suggests a magnetic character. The projected density of states is shown in Fig. 8(b). It confirms the metallic character, and the difference between spin-up and spin-down channels, although very small, together with the results of magnetic moment analysis, suggest a ferrimagnetic character. The band of sulfur appears to be hybridized with that of metals, and no bandgap is observed near E_F. We calculated the total magnetization to be 2.671 μ_B per metal ion, where the contribution of each metal is −0.04 μ_B per iron ion, 0.244 μ_B per cobalt ion, 2.469 μ_B per nickel ion, and −0.029 μ_B per copper ion. Here, the contribution to the magnetic moment comes essentially from Ni^{2+} cations. Therefore, the calculation result reported here supports the experimental observations.

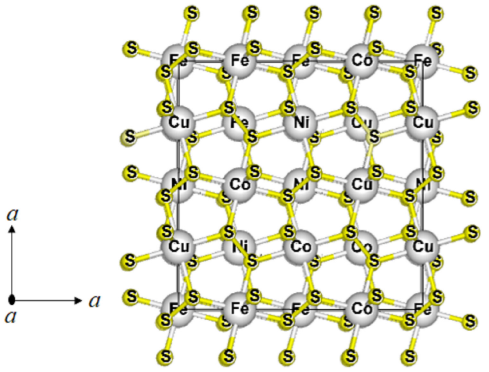

Fig. 7. (Color online) Crystal structure model of (Fe, Co, Ni, Cu)S$_2$ from DFT calculation, visualized using VESTA software.

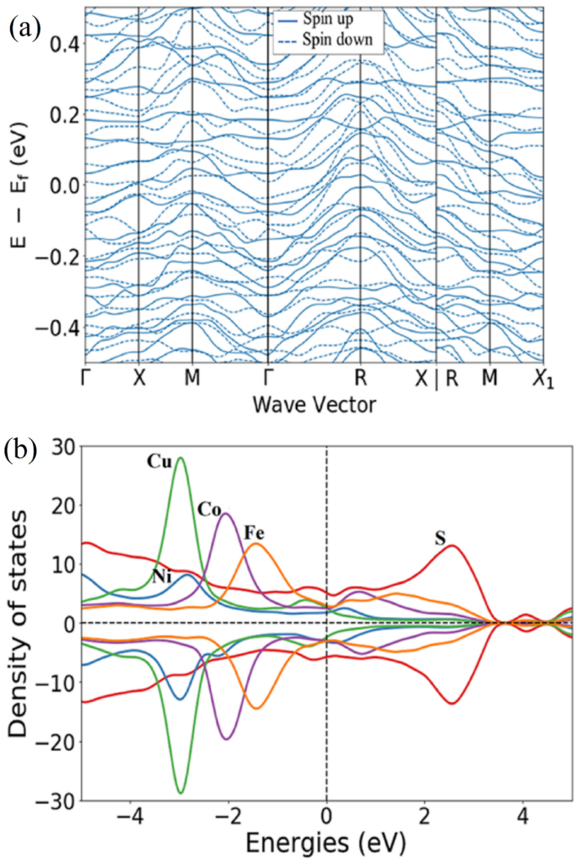

Fig. 8. (Color online) (a) Band electronic structure and (b) projected density of states of (Fe, Co, Ni, Cu)S$_2$.

As we explained in the introduction, FeS$_2$ is a diamagnetic semiconductor with the electrons of Fe^{2+} ($t_{2g}^6 e_g^0$) completely filled at t_{2g} and empty at e_g states, which overlap with the sulfur atom electronic states at the conduction band.[15] This configuration is qualitatively similar to that of RuS$_2$.[21] On the other hand, CoS$_2$ shows a half-metallic ferromagnetism owing the Co^{2+} ($t_{2g}^6 e_g^1$) electron in the e_g band.[17] NiS$_2$ is a Mott-insulator antiferromagnet with the d electrons' configuration of Ni^{2+} ($t_{2g}^6 e_g^2$), the band gap of NiS$_2$ can be described as a half-filled e_g.[18,34] CuS$_2$ is metallic because the Cu^{2+} ($t_{2g}^6 e_g^3$) electrons occupy the e_g band and becomes a superconductor at $T_c = 1.5$ K.[19] In addition, two-metal disulfide solid solutions with pyrite structure have also been reported, where the substitution of Co or Cu in Ni site of NiS$_2$

©2022 The Author(s)

J. Phys. Soc. Jpn.
Downloaded from journals.jps.jp by 138.25.168.236 on 11/21/22

could decrease or increase the number of electrons in the half-filled e_g board band.[22] These results support the assumption that the electrons from the p state of sulfur might be eliminated by inserting of more electronegative elements, which are expected to affect the physical properties of the material.[35] Our results are in line with those in the references, where Ni^{2+} may largely contribute to the ferrimagnetic character of our compounds. In contrast, the contributions of Fe^{2+}, Co^{2+}, Cu^{2+}, and Ru^{2+} are significantly smaller.

4. Conclusions

We successfully stabilized high entropy metal disulfides (Fe, Co, Ni, Cu)S_2 and (Fe, Co, Ni, Cu, Ru)S_2 into a single-phase pyrite-type structure by applying high pressure and high temperature. The crystal structure of the high-entropy metal disulfides (Fe, Co, Ni, Cu)S_2 was determined by single-crystal X-ray diffraction analysis. It crystallizes in a pyrite-type structure with space group $Pa\bar{3}$ (#205) and lattice parameter $a = 5.5777(3)$ Å, where all metal atoms randomly occupy the cation site. The property, both with and without Ru atom, is metallic with a ferrimagnetic character below $T_c = 130$ K. The DFT calculations confirm the metallic and ferrimagnetic properties and suggest a large magnetic contribution from Ni.

Acknowledgements This study was supported by KAKENHI, Grant-in-Aid for Scientific Research on Innovative Areas (#18H05456, #18H05462), Scientific Research (A) (#18H03692), and Scientific Research (C) (#20K05450), as well as by the GRIMT program (#202012-RDKGE-0065) at the Institute for Materials Research, Tohoku University. Some of the measurements of physical properties were performed at CEMS, RIKEN, and Techno-plaza at Shibaura Institute of Technology.

---

*Corresponding author: ayako@shibaura-it.ac.jp

1) B. Cantor, I. T. H. Chang, P. Knight, and A. J. B. Vincent, Mater. Sci. Eng. A **375–377**, 213 (2004).
2) J. W. Yeh, S. K. Chen, S. J. Lin, J. Y. Gan, T. S. Chin, T. T. Shun, C. H. Tsau, and S. Y. Chang, Adv. Eng. Mater. **6**, 299 (2004).
3) L. Chmielak, L. M. Roncery, P. Niederhofer, S. Weber, and W. Theisen, SN Appl. Sci. **3**, 835 (2021).
4) C. M. Rost, E. Sachet, T. Borman, A. Moballegh, E. C. Dickey, D. Hou, J. L. Jones, S. Curtarolo, and J. P. Maria, Nat. Commun. **6**, 8485 (2015).
5) D. Bérardan, S. Franger, A. K. Meenab, and N. Dragoe, J. Mater. Chem. A **4**, 9536 (2016).
6) Z. Teng, L. Zhu, Y. Tan, S. Zeng, Y. Xia, Y. Wang, and H. Zhang, J. Eur. Ceram. Soc. **40**, 1639 (2020).
7) R. Z. Zhang, F. Gucci, H. Zhu, K. Chen, and M. J. Reece, Inorg. Chem. **57**, 13027 (2018).
8) T. X. Nguyen, Y. H. Su, C. C. Lin, and J. M. Ting, Adv. Funct. Mater. **31**, 2106229 (2021).
9) L. Lin, K. Wang, A. Sarkar, C. Jiel, G. Kakera, Q. Wang, R. Azmi, M. Fichtner, H. Hahn, S. Schweidler, and B. Breitung, Adv. Energy Mater. **12**, 2103090 (2022).
10) T. Ying, T. Yu, Y. S. Shiah, C. Li, J. Li, Y. Qi, and H. Hosono, J. Am. Chem. Soc. **143**, 7042 (2021).
11) D. J. Vaughan, Rev. Mineral. Geochem. **61**, 1 (2006).
12) C. Arrouvel and J. G. Eon, Mater. Res. **22**, 1 (2018).
13) S. Jobic, P. Deniard, R. Brec, J. Rouxel, M. G. B. Drew, and W. I. F. David, J. Solid State Chem. **89**, 315 (1990).
14) H. E. King, Jr. and C. T. Prewitt, Am. Mineral. **64**, 1265 (1979).
15) C. I. Pearce, R. A. D. Pattrick, and D. J. Vaughan, Rev. Mineral. Geochem. **61**, 127 (2006).
16) S. A. J. Kimber, A. Salamat, S. R. Evans, H. O. Jeschkle, K. Muthukumar, M. Tomic, F. S. Pujol, R. Valenti, M. V. Kaisheva, I. Zizak, and T. Chatterji, Proc. Natl. Acad. Sci. U.S.A. **111**, 5106 (2014).
17) A. Teruya, F. Suzuki, D. Aoki, F. Honda, A. Nakamura, M. Nakashima, Y. Amako, H. Harima, K. Uchima, M. Hedo, T. Nakama, and Y. Ōnuki, J. Phys.: Conf. Ser. **807**, 012001 (2017).
18) Y. Feng, R. Jaramillo, A. Banerjee, J. M. Honig, and T. F. Rosenbaum, Phys. Rev. B **83**, 035106 (2011).
19) M. Kakihana, T. D. Matsuda, R. Higashinaka, Y. Aoki, A. Nakamura, D. Aoki, H. Harima, M. Hedo, T. Nakama, and Y. Ōnuki, J. Phys. Soc. Jpn. **88**, 014702 (2019).
20) T. A. Bither, R. J. Bouchard, W. H. Cloud, P. C. Donohue, and W. J. Siemons, Inorg. Chem. **7**, 2208 (1968).
21) R. Bichsel, F. Levy, and H. Berger, J. Phys. C **17**, L19 (1984).
22) A. Maignan, R. Daou, E. Guilmeau, D. Berthebaud, T. Barbier, O. Lebedev, and S. Hébert, Phys. Rev. Mater. **3**, 115401 (2019).
23) H. Wang, H. Ma, B. Duan, H. Geng, L. Zhou, J. Li, X. Zhang, H. Yang, G. Li, and P. Zhai, ACS Appl. Energy Mater. **4**, 1610 (2021).
24) M. Tokuda, K. Yubuta, T. Shishido, and K. Sugiyama, Acta Crystallogr., Sect. E **78**, 76 (2022).
25) G. M. Sheldrick, Acta Crystallogr., Sect. A **71**, 3 (2015).
26) G. M. Sheldrick, Acta Crystallogr., Sect. C **71**, 3 (2015).
27) C. Schuster, M. Gatti, and A. Rubio, Eur. Phys. J. B **85**, 325 (2012).
28) R. D. Shannon, Acta Crystallogr., Sect. A **32**, 751 (1976).
29) (Supplemental Material, Table S1) Experimental details of X-ray single-crystal structure refinement is provided online.
30) T. Itoh, M. Inukai, N. Kitamura, N. Ishida, Y. Idemoto, and T. Yamamoto, J. Mater. Chem. A **3**, 6943 (2015).
31) N. Elliott, J. Chem. Phys. **33**, 903 (1960).
32) (Supplemental Material, Fig. S1) Temperature-dependent inverse magnetic susceptibility is provided online.
33) S. Blundell, *Magnetism in Condensed Matter* (Oxford University Press, New York, 2001) Chap. 3, p. 49.
34) S. E. Khatib, B. Voigt, B. Das, A. Stahl, W. Moore, M. Maiti, and C. Leighton, Phys. Rev. Mater. **5**, 115003 (2021).
35) K. Ramesha and R. Seshadri, Phys. Rev. B **70**, 214409 (2004).

©2022 The Author(s)